Proceedings World Geothermal Congress 2026
Calgary, Canada, June 8 – 11, 2026

Constant micro-seismic event rate loading can minimise induced micro-seismicity in a deforming porous rock: Insights from a sound and vision experiment

Maria-Daphne Mangriotis[1,3], Alexis Cartwright-Taylor[2,3]*, Ian G. Main[3], Ian B. Butler[3], Andrew Curtis[3], Florian Fusseis[4], Andrew Bell[3]

[1]National Oceanography Centre, UK, [2]Heriot-Watt University, UK, [3]University of Edinburgh, UK, [4]RWTH Aachen University, Germany, *a.cartwright-taylor@hw.ac.uk

Keywords: Induced seismicity, Micro-seismicity, X-ray microtomography, Rock deformation, Sub-critical failure

INTRODUCTION

Subsurface activities such as geothermal energy production involve extraction and injection of fluids, which disturbs tectonic stresses in the Earth's crust. Subsurface ruptures, and associated seismicity, induced by such stress perturbations carry a risk of damage from ground motion, of fluid leakage to the surface due to increased flow pathways, and of potential loss of public confidence. Safe operation of these activities therefore requires effective management to minimise induced seismicity. Currently, this involves using a 'traffic light' system based on the maximum magnitude of recorded seismic events. Operations may continue as planned (green), be modified (amber), or suspended (red) depending on the pre-set magnitude threshold. However, such systems can be unreliable, with magnitudes continuing to increase even after cessation of operations due to reactive controls being evoked too late in the process, with potentially catastrophic economic and societal effects.

In geothermal energy operations, managing induced seismicity is a critical challenge. In Enhanced Geothermal Systems (EGS) the hydraulic fracturing required to generate permeable fracture networks in deep crystalline basement rocks involves larger pressures during injection and smaller fluid volumes than low-pressure, long-term applications such as carbon capture and storage (CCS). As a result, there are several cases of large jumps in seismicity, even after cessation of operations. For example, the South Korea Pohang M_w 5.5 event (Grigoli et al., 2018), and the induced seismic sequences detected at Soultz-sous Forêts (Foulger et al., 2018). The Basel geothermal project was closed altogether due to public opposition after induced seismic events as large as M_w 3.4 were felt by the local population (Häring et al., 2008). Recent studies have shown that, instead of waiting for the thresholds, when it may be too late, maximum magnitudes can be limited if the injection protocol is varied continuously; for example to constrain the amount of stored elastic energy available for rupture propagation (Kwiatek et al., 2019), or with cyclic pressurization and pulse pumping (Zang et al., 2019).

An early alternative risk management approach deployed in mining operations used continuous micro-seismic event rate monitoring to identify periods of higher risk of rockbursts, outbursts, and other catastrophic failures, ceasing activity and evacuating mines for a critical threshold of 100 events per day (Styles et al., 1991). This protocol enabled the mine to be worked for four years without any such major events or associated fatalities (Styles et al., 1993), proving that micro-seismic event rate could serve as a suitable control parameter at field scale. Terada et al. (1984) had already demonstrated this possibility on a smaller scale in the laboratory; by adjusting the load to maintain a constant micro-seismic event rate they slowed deformation and prevented the transition from stable crack propagation to unstable dynamic rupture. This protocol was used effectively to promote and capture quasi-static fault nucleation and propagation by mapping acoustic emission event locations (Lockner et al., 1991) and associated microstructural changes with in-situ X-ray microtomography (Cartwright-Taylor et al., 2022).

Here, we seek to explain the mechanism by which feedback control on the micro-seismic event rate works to stabilize rock failure, promote sub-critical crack growth and reduce the associated micro-seismicity, including the maximum magnitude (Mangriotis et al., 2025). We propose a new model, based on the observed evolution of microstructural damage and the fracture mechanics of subcritical crack growth (Meredith and Atkinson, 1983; Main, 2000), to explain how constant micro-seismic event rate stabilizes failure and reduces seismic hazard. We then test the model on experimental data for constant event rate loading (Cartwright-Taylor et al., 2022) and isolate the effects of event rate feedback control with a benchmark constant strain rate experiment. Uniquely, these experiments combine acoustic monitoring and feedback control with contemporaneous in-situ X-ray microtomography of the microstructure and were conducted in our X-ray transparent rock deformation apparatus Stor Mjölnir (Cartwright-Taylor et al., 2022). We test the following hypotheses: (1) stress history for constant event rate control can be described by the new sub-critical model; (2) microstructural deformation

mechanisms are different between the two loading protocols; (3) the number of micro-seismic events is lower under constant event rate control and the micro-seismic *b*-value remains relatively constant throughout.

1 MODEL THEORY AND DEVELOPMENT

During compressional failure, local strains comprise both tensile and shear mechanisms which are highly correlated and transition from predominantly tensile to predominantly shear as the bulk mechanical behavior transitions from strain hardening after yield to strain softening after peak stress (Cartwright-Taylor et al., 2022). Our model assumes that the empirical relationship Charles' law observed during tensile loading (Meredith and Atkinson, 1983) also applies for compressional failure, while accommodating the additional local hardening due to crack arrest typically observed under compression (Main, 2000). The model is derived in detail in Mangriotis et al. (2025), and we summarize it here. We take the stress intensity, or crack extension force, K to be an effective mean field parameter, used previously to explain event rate and *b*-value evolution under increasing differential stress (Main, 1991) and the emergence of power-law brittle creep under constant load (Main, 2000).

The representative crack growth velocity, V, of the ensemble of fractures and the micro-seismic event rate, $\dot{N}$, are assumed to be related to the stress intensity factor, K, by Charles' law, where $n > 2$ and remarkable similar for the two relationships (Meredith and Atkinson, 1983): $V = V_c(K/K_c)^n$and $\dot{N} = \dot{N}_c(K/K_c)^n$, implying that event rate is an indirect measure of crack growth velocity. V_c and $\dot{N}_c$ are the critical values at the point of dynamic rupture, while K_c is the fracture toughness and n is the stress corrosion index. For single mode failure, $K_i = Y\sigma c^{1/2}$, where σ is the differential stress, c is a representative crack length and Y is a dimensionless scaling factor. In the general mixed-mode case, we allow the exponent, which we denote q, to differ from ½ so that Y does have dimensions. Softening (shear) and hardening (tensile) processes are described simply as $K_i = Y\sigma c^{q_s}$ and $K_i = Y\sigma c^{-q_h}$ respectively, where q_s and q_h are both positive. The negative sign then implies negative feedback, inhibiting tensile crack growth by reducing K as c increases, while the positive sign implies positive feedback, promoting localized shear processes during failure along a deformation band.

Using a boundary condition of constant $\dot{N}$, we assume a linear superposition of the two processes with a time-dependent weighting function for the transition. In this case, K and V are also constant, while σ and c are both functions of time: $\sigma = \sigma(t)$ and $c = c_0 + Vt$. So, for a softening process, $K = Y\sigma(t)(c_0 + Vt)^{q_s} = A\sigma(t)(1 + t/T_s)^{q_s}$, where $A = Yc_0^{q_s}$is a constant, and the characteristic softening time $T_s = c_0/V$. For constant K, $\sigma(t) = \sigma_0(1 + t/T_s)^{-q_s}$. Similarly, for hardening $\sigma(t) = \sigma_0(1 + t/T_h)^{q_h}$. We allow T_s and T_h to be independent variables. We apply a further boundary condition to account for $\sigma \to \sigma_F$ as $t \to \infty$, where σ_F is the steady state frictional sliding stress after the fault has fully developed: $\sigma(t) = \sigma_F + (\sigma_0 - \sigma_F)(1 + t/T_s)^{-q_s}$ (and similar for hardening). In the case of small σ_F, the mixture model can be expressed as:

$$\sigma(t) = \sigma_0[\omega(t)(1 + t/T_h)^{q_h} + [1 - \omega(t)]1 + t/T_s)^{-q_s}] \quad (1)$$

where the evolving weighting function for the transition from hardening to softening $\omega(t) = e^{-t/T_w}$ and T_w is its characteristic waiting time.

2 EXPERIMENTAL MATERIAL, APPARATUS AND PROTOCOL

We conducted a set of two rock compression experiments on water-saturated Clashach sandstone, comparing the two loading protocols: conventional constant axial strain rate loading (Test A), and constant micro-seismic event rate loading (Test B). The experimental setup, testing procedure and types of data acquired are described in detail in Mangriotis et al. (2025) and Cartwright-Taylor et al. (2022).

Clashach sandstone is a Permian aeolian sandstone from Morayshire, Scotland. It is a well-sorted quartz-rich (>92% quartz) arenite, highly cemented with grain size 250-400μm. The triaxial compression experiments were conducted in our X-ray transparent rock deformation apparatus, Stor Mjölnir, made from grade 5 Ti alloy with a 7068-T6 aluminium alloy X-ray transparent pressure vessel, installed on the Xray microtomography rotation stage in Experimental Hutch 1 of beamline I12:JEEP at the UK Diamond Light Source. Cylindrical samples 10mm diameter and 25mm long were cored with a diamond-tipped core drill and then the ends ground flat and parallel on a lathe. The samples were jacketed in silicone tubing and placed between two pistons with axially-located piezoelectric transducers located at the other end of each piston. An acoustic couplant (silicon grease or a honey-like molasses) was used to ensure good transmission of acoustic waves over a wide range of frequencies.

The experiments were performed at room temperature under water-saturated, drained conditions with deionized water as the pressurizing fluid. The confining and pore fluid pressures, 25 MPa and 5 MPa respectively, were held constant throughout the test. Once a hydrostatic starting condition was achieved, the samples were loaded continuously at a constant axial strain rate of 10^{-5} s^{-1}. This rate was maintained until failure for Test A,

while for Test B, the loading protocol switched to constant micro-seismic event rate control, regulating the applied stress throughout failure by slowing down the stroke rate of the ram or even allowing it to go slightly into reverse to maintain the event rate at 1±1 event/s. This extended the failure time from ~1 min to ~ 50 min (bulk average strain rate of 10^{-7} s^{-1}). Acoustic emission (AE) events were recorded continuously during loading. The pre-amplification gain was increased from 60dB (Test A) to 70dB (Test B) to maximize signal to noise in the electronically noisy synchrotron hutch, after the learning experience of test A. This meant that we could not pick as many low amplitude events in Test A as in Test B. Test A event waveforms (along with noise) were re-scaled to 70dB, to ensure compatibility of both sets of results for a fair comparison, at the expense of a higher magnitude detection threshold. X-ray imaging was achieved with a 53eV monochromatic beam. Reconstructed tomographic volumes, with voxel size 7.91 μm^3, of the whole sample were obtained every 85s. Digital volume correlation between neighboring pairs of tomographic volumes produced incremental 3D local strain fields.

3 RESULTS

Hypothesis 1 was validated: Stress history for constant event rate control was consistent with the new sub-critical model. Figure 1 shows the differential stress history and bulk stress-strain relationship. Due to natural sample variability, the sample in Test A was less stiff than in Test B, experiencing a lower differential stress through more dynamic post yield loading conditions, even though the evolution of the mean internal strain was similar between the samples and the work done was greater in Test A. The model fit for Equation (1) is shown in green. We fixed t_0 as the onset time of event rate loading, with $\sigma_0 = \sigma(t = 0)$. We also assumed $q_s = q_h = \frac{1}{2}$, and $\sigma_F = 0$. The free parameter vector is then (T_h, T_s, T_ω). Our new theory is validated to a high degree of precision ($r = 99\%$) by experimental data not involved in formulating the hypothesis. For Test B, the effective medium crack velocity, $V = [c_{max} - c_{min}]/T_d$, estimated from the observed maximum (800μm) and minimum (18μm) crack lengths, c_{max} and c_{min} respectively, and the duration of the event rate control, $T_d = 3600$s, stabilized at $V = 0.217$μm/s.

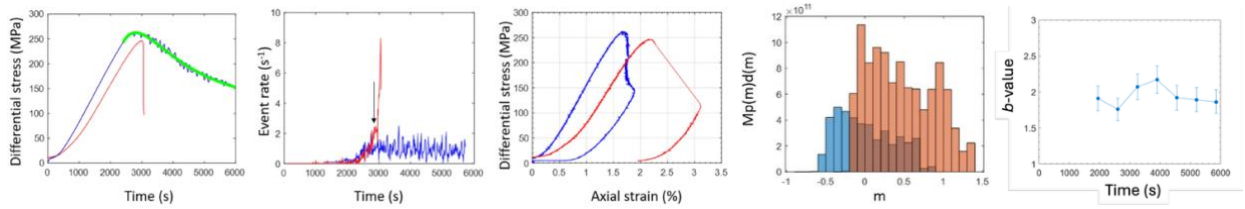


Figure 1. Left to right for Test A (red) and Test B (blue): stress history with model fit for Test B in green; event rate history; stress-strain relationship; weighted micro-seismic moment distribution; *b*-value evolution.

Hypothesis 2 was validated: Deformation mechanisms are different between the two loading protocols, although there were some similarities between tests. Figure 2 shows the evolution of incremental dilation and shear strain fields from just before yield to peak stress. Figure 3 shows example greyscale tomographic slices at peak stress (left) and post-failure (right). In both samples, dilation and shear are strongly correlated and strain clustering begins in the bottom left and top right edges. Cracks nucleate from the edges of pores, as wing cracks and as Hertzian contact cracks, and localization is apparent as en-echelon tensile microcracks. However, localization along the eventual failure plane of both local strain and en-echelon tensile cracks occurs earlier in Test A (during strain hardening immediately before peak stress and at peak stress respectively) than in Test B. Test B exhibits exploratory strain localization along several candidate shear zones until the final shear zone emerges after peak stress (during strain softening), with localized en-echelon tensile cracks appearing immediately following this strain increment. In both cases, localized en-echelon microcracks first appear in the greyscale tomographic slice immediately following the failure plane localization strain increment. Post-failure, the two tests exhibited significant differences, with Test B (event rate control) showing: higher residual stress; smaller proportion of damaged rock; narrower shear zone; shorter and less open microcracks; less branching of the shear zone; less cataclasis, gouge and porosity, and fewer intergranular cracks, within the shear zone than Test A (strain rate control). However, synthetic and antithetic sliding and fragment rotation in the shear zone was evident in both samples.

Hypothesis 3 was validated: The number of micro-seismic events is lower under constant event rate control and the micro-seismic *b*-value remains relatively constant throughout. Several significantly larger AE events were recorded during Test A than Test B, associated with an acceleration in the average local dilation and shear strains after the loading protocol diverged between the two tests. A similar acceleration to failure was seen in the AE event rate for Test A. Total recorded events were 2235 and 3660 for tests A and B respectively. Figure 1 shows the event rate evolution, incremental frequency vs seismic magnitude distribution weighted by the seismic

moment and *b*-value evolution. We observe smaller maximum magnitudes and a smaller number of events of all sizes. The difference in total number of events recorded was due to the differences in gain used between the tests, whereby more small events were detected during Test B than Test A. Estimated overall *b*-values above the completeness magnitude were similar between tests: 1.86 ± 0.06 and 1.94 ± 0.04 for test A and B respectively, although considered significantly larger for Test A according to the Welch unpaired test. Temporal evolution of *b*-value for Test A shows that it remains constant within error throughout the experiment.

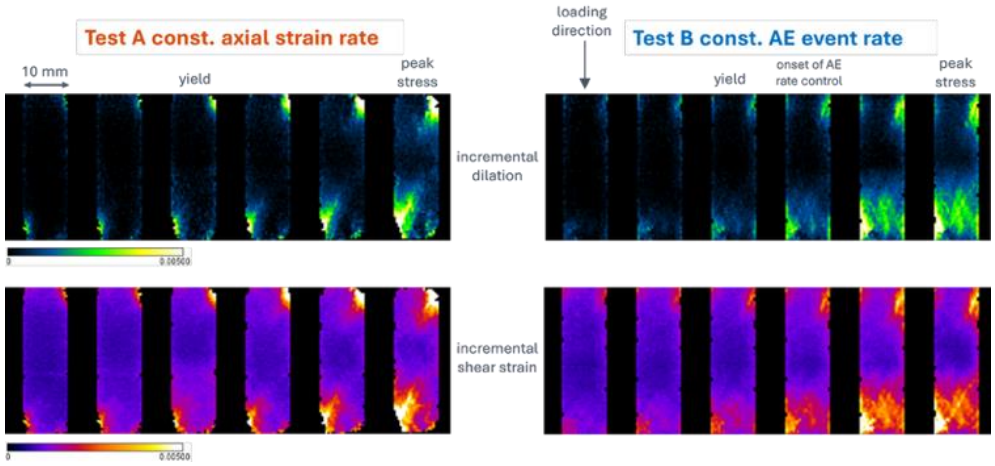


Figure 2. 2D median along-strike projections of 3D incremental dilation and shear strain fields.

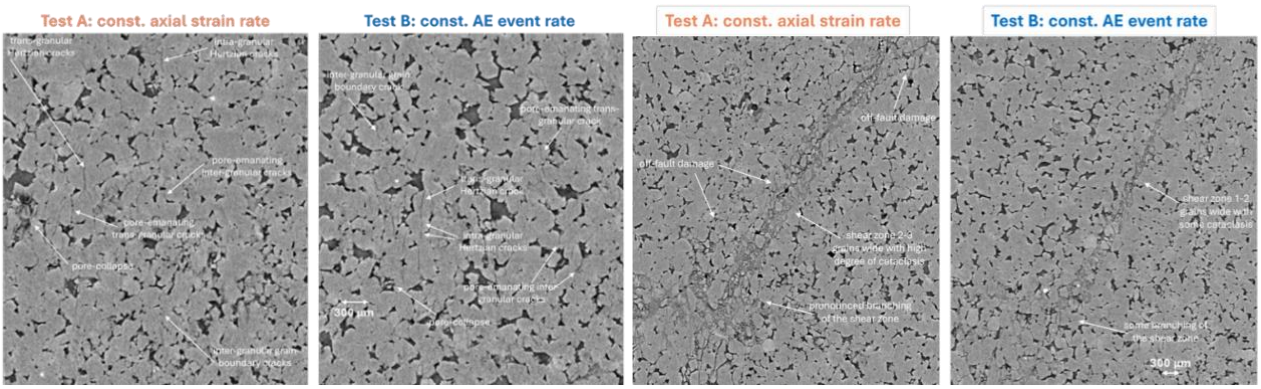


Figure 3. 2D greyscale slices showing similar crack nucleation mechanisms in each sample at peak stress (LEFT) and post-failure after unloading (RIGHT).

4 DISCUSSION AND CONCLUSIONS

Our main findings validate the three hypotheses set out in the introduction, including validating our fracture mechanics mixture model for event rate control to high precision, providing a theoretical basis for the effectiveness of the control for stabilizing deformation and preventing runaway dynamic rupture seen in Test B. By maintaining the event rate within a narrow range, the inferred effective mean field stress intensity is maintained constant within an even narrower range according to Charles' law. If control is lost, Charles' law predicts a power-law acceleration of event rate to failure, as seen in Test A. The temporally constant *b*-value observed for Test B (within error) provides further evidence for the constant stress intensity mechanism, since there is, in general, a negative correlation between *b*-value and stress intensity (Meredith et al., 1990). The slightly lower overall b-value for Test B than Test A is also consistent with the stress intensity control hypothesis, implying a lower overall stress intensity and a reduction in the likelihood of extreme events for Test B.

Most of the observed differences in the microstructure of the eventual shear zone can be explained by slower strain accumulation and a slower rupture rate, while the fundamental micromechanics of crack nucleation, strain/crack localization and grain fragmentation and rearrangement in the shear zone were similar between samples. These differences include a smaller proportion of damaged rock, less fragmentation and gouge, delayed onset of localization and a narrower shear band in Test B. Event rate control leads to suppression of maximum magnitudes by almost an order of magnitude and a smaller number of events of all sizes. Similar AE corner frequencies and inferred crack sizes were seen in the ten largest events across both tests, indicating that rupture velocities for individual dynamic micro-fracturing events were similar. When combined with the smaller

inferred seismic moments observed in Test B, this implies that event rate control promotes smaller stress drops, thereby inhibiting run-away failure.

Although fluid-induced seismicity has a time-delay associated with fluid diffusion away from the wellbore, AE feedback control response time in a small, relatively permeable system in the lab is fast enough to provide effective control. This may extrapolate to field conditions where permeability is high and/or the distance to the critically stressed faults and fractures is small. This hypothesis has been proven in at least one case by Kwiatek et al (2019), who showed that extreme events can be controlled at field-scale during EGS operations in heavily folded, foliated, jointed, and faulted crystalline basement rocks. This demonstrator achieved a relatively constant seismic event rate by modulating the fluid injection, even though they did not intentionally adjust the injection rate to maintain a constant seismic event rate. Hence, seismic event rate control may be effective for managing the risk from fluid-induced seismicity in other field settings where similar conditions are met.

Acknowledgements

We thank Alex Hart and Ivan Febbrari of the University of Edinburgh Geosciences Mechanical Workshop for their support in manufacturing the experimental apparatus. We also acknowledge Diamond Light Source for time on beamline I12-JEEP under proposal MG22517. We thank beamline scientist Oxana Magdysyuk for her contributions to x-ray tomography acquisition. This work was supported by the UK's Natural Environment Research Council (NERC) through the CATFAIL project NE/R001693/1 Catastrophic failure: what controls precursory localisation in rocks?

REFERENCES

Cartwright-Taylor, A. et al. (2022). Seismic events miss important kinematically governed grain scale mechanisms during shear failure of porous rock. *Nat. Commun.* **13**, (2022), 6169.

Foulger, G.R. et al., Global review of human-induced earthquakes. *Earth Sci. Rev.* **178**, (2018), 438–514.

Grigoli, F. et al. The November 2017 Mw 5.5 Pohang earthquake: a possible case of induced seismicity in South Korea. *Science* **360**, (2018), 1003–1006.

Häring, M.O. et al. Characterisation of the Basel 1 enhanced geothermal system. *Geothermics*, **37(5)**, (2008), 469e95.

Kwiatek, G. et al. Controlling fluid-induced seismicity during a 6.1-km-deep geothermal stimulation in Finland. *Sci. Adv.* **5**, (2019), eaav7224.

Lockner, D. et al. Quasi-static fault growth and shear fracture energy in granite. *Nature* **350**, (1991), 39–42

Main, I.G. A damage mechanics model for power-law creep and earthquake aftershock and foreshock sequences. *Geophys. J. Int.* **142**, (2000), 151–161.

Main, I.G. A modified Griffith criterion for the evolution of damage with a fractal distribution of crack lengths: application to seismic event rates and b-values. *Geophys. J. Int.* **107**, (1991), 353–362.

Mangriotis, M.D. et al. Loading of a porous rock with constant micro-seismic event rate suppresses seismicity and promotes subcritical failure. *Sci. Rep.* **15**, (2025), 19351.

Meredith, P.G. and Atkinson, B.K. Stress corrosion and acoustic emission during tensile crack propagation in Whin sill dolerite and other basic rocks. *Geophys. J. Roy. Astron. Soc.* **75**, (1983), 1–21.

Meredith, P.G. et al. Temporal variations in seismicity during quasi-static and dynamic rock failure. *Tectonophys.* **175**, (1990), 249–268.

Styles, P. et al. Implications of harmonic-tremor precursory events for the mechanism of coal and gas outbursts. *Proceedings*, 3rd International Symposium on Rockbursts and Seismicity in Mines, Kingston, Ontario, Canada (1993), 415–421.

Styles, P. et al. Microseismic prediction and control of coal outbursts in Cynheidre Colliery. *Proceedings*, 5th Conference Acoustic Emission / Microseismic Activity in Geological Structures and Materials, ed. Hardy, *Trans. Tech. Publications*, (1991), 265–274.

Terada, M. et al. AE rate-controlled compression test of rocks. *Proceedings*, 3rd Conference on Acoustic Emission / Microseismic Activity in Geologic Structures and Materials, eds. Hardy and Leighton, *Trans. Tech. Publications*, (1984), 159–171.

Zang, A. et al. How to Reduce Fluid-Injection-Induced Seismicity. *Rock Mech. Rock Eng.* **52**, (2019), 475–493.